Design, Processing and Testing of A MEMS Energy Grooming Structure for Initiator Materials

HENGZHEN FENG [ID] [1], (Member, IEEE), WENZHONG LOU[1], FUQUAN ZHENG[1], (Member, IEEE), AND XURAN DING [2], (Member, IEEE)

[1]National Key Laboratory of Electro-Mechanics Engineering and Control, School of Mechatronical Engineering,
Beijing Institute of technology, Beijing CO100081, China
[2]China North Industries Corporation, Beijing CO100053, China

Corresponding author: Hengzhen Feng (fenghengzhen@gmail.com)

ABSTRACT A common problem experienced by micro-electro-mechanical system (MEMS) initiators is unintentional triggering in a transient high-pulse environment owing to low ignition energy. Herein, therefore, combining the size effect of the Paschen's law with a modified semi-empirical formula of the secondary electron emission coefficient, a theoretical calculation was carried out to improve the electrostatic grooming structures. It was found that the size effect of the Paschen's law is owing to the distance-dependent process dominance of the Thomson discharge process and the field-induced electron emission process. A microscale breakdown model was, thus, proposed based on field-induced electron emission and the secondary electron emission coefficient. The structural simulations and the optimization of various materials were carried out using the multiphysics field simulation software (i.e., COMSOL), and an electrostatic grooming device was subsequently fabricated. During experimental testing, the transient voltage of an electrostatic grooming device with a 1 μm-wide comb gap could be groomed over 130 V. Furthermore, the model was in good agreement with the experimental results in the range of less than 2 μm and more than 9 μm. In the optimum range of 2–9 μm, the result of the test differed from the model by less than 15%. The model, therefore, possesses excellent adaptability in this scale range and can be used to greatly improve the antistatic characteristics of initiators.

INDEX TERMS Antistatic characteristic, energy grooming, field-induced electron emission process, Paschen's Law, secondary electron emission.

I. INTRODUCTION

The initiator of a micro-electro-mechanical system (MEMS) device possesses a low ignition energy, and thus its electrostatic protection has become a technical problem that must be solved in the MEMS fuse. Over the years, institutions have carried out a great deal of research work in this field. Electrostatic protection mainly prevents an initiator foot–foot or foot–shell electrostatic discharge that would result in an accidental trigger of the initiator [1]. The main technical methods for electrostatic protection have been increasing the cross-sectional area of the initiators and changing the physical characteristics, such as by forming ignition bridges with doped semiconductor materials [2]–[4]. In many electrostatic

protection measures, a transient-voltage-suppression (TVS) diode is used to absorb transient energy. In this function, the TVS effectively absorbs the electrostatic energy and releases a large amount of current instantaneously, thus enabling energy channeling [5]–[9]. During electrostatic protection, the internal P-N junction is in a reverse bias state. In a certain voltage range, at the end of the P-N junction a small leakage current flows through TVS, which exhibits a high impedance state. The internal electric field of the P-N junction is very strong, and when the reverse voltage is higher than the reverse breakdown voltage of the P-N junction, a few carriers are subjected to this strong electric field. In this way a large amount of energy is obtained by the carriers, which collide with other atoms to form new electron-hole pairs. As the carrier number increases, more carriers can collide to form more electrons under the action of this strong electric field, and the

electron-hole pairs will cause a chain reaction resulting in a rapid increase of the reverse current. Under these conditions, the TVS exhibits a low impedance state and absorbs a large amount of the pulse power. The voltage clamp between the two poles is placed at a predetermined value and, using the avalanche breakdown characteristic of the TVS, electrostatic discharge protection can be realized. However, owing to the impedance and fabrication problems of the TVS tube itself, its energy absorption performance is limited [7], [10]–[14].

In this paper, a novel MEMS electrostatic grooming structure based on the size effect of Paschen's law is proposed. Adopting the design idea of hydrophobic electrostatic charge structures and using MEMS technology to design the micro-discharge electrode apparatus, we attempt to design a structure that can reliably break down at a lower voltage threshold and release the static charge that accumulates between the initiator pins or the pin and the TVS tube and shell. This can effectively groom any static electricity, radio frequency or other adverse environmental stimuli and thus increase the initiator protection. Further, through parameterization and serialization it is possible to design and improve the electrostatic characteristics of the initiator [15].

Protection from static electricity can be achieved only by effectively connecting the electrostatic groomer with the circuit and structure that requires an antistatic condition. Unlike the requirements of constant current grooming structures for solid-state protection, the electrostatic grooming structure does not require external control signals. Its special working principle guarantees that it can only groom abnormal voltage signals at both ends of the explosive device initiator, but has no effect on the normal driving energy of the pyrotechnic products.

II. THEORY AND DESIGN: DESIGN OF ELECTROSTATIC GROOMING STRUCTURE BASED ON THE SIZE EFFECT OF PASCHEN'S LAW

In the design development of electrodes for technological application at the microscale, nonmetallic electrode materials (i.e., doped polysilicon) exhibit a Paschen's curve in good agreement with the experimental results [17]. However, when the gap distance of metal electrodes is less than 10 μm, the experimental results are inconsistent with the classical Paschen's law. Therefore, research regarding the size effect and modification of Paschen's law are underway.

Air breakdown consists of the two main physical processes of Thomson discharge and field emission, where each process exerts a different dominance at different size scale ranges. Specifically, Thomson discharge dominates in the breakdown process with gaps greater than 7 μm, the two processes are comparable in a gap range of 4–7 μm, and field emission dominates with gaps less than 4 μm [18]. Field emission refers to the reduction and thinning of the surface energy barrier when the solid material surface is strengthened by an electric field. When the barrier thickness is reduced to the order of magnitude of the electron wavelength, a large number of electrons at the Fermi level are able to escape

from the barrier. The field emission of electrons is actually quite complicated, so a precise physical analytical model has not yet been proposed. The complication exists mainly in the need to solve the Schrodinger equation of the electron potential energy function in the process of solving the electron emission current density. Therefore, the field emission theory of electrons is typically solved using the approximation method of field emission theory, where Fowler and Nordheim (FN) proposed the field emission theory of metal electrons [16]. Herein, the expression of the field emission current density of electrons, j_{FN}, was simplified as

$$j_{FN}(0) = A_{FN} E^2 \exp(-\frac{B_{FN}}{E}) \qquad (1)$$

where A_{FN} and B_{FN} are constants and E is the electric field intensity. The conditions of simplification for Eq. (1) that ensure a universal and optimum approximation are that absolute zero is used as the boundary condition and the temperature of the electrode should not be higher than 1000K. Herein, the electrode temperature was less than 1000K, so this formula could be used as the basis of the calculation.

In this work, we conclude that the relation between the field emission current density and the applied electric field basically satisfies the requirement of $j_{FN}(0) \propto \exp(-1/E)$ because the first term in Eq. (1) (i.e., E^2) is dominated by the second term (i.e., $\exp(-1/E)$).

For the discharge existing between parallel substrates at the microscale, the electric field produced by the space charge of a positive ion will be superposed with the external electric field when a charged positive ion hits the cathode. This will form a very strong local electric field that will enhance the field emission effect. Experiments have demonstrated that the electric field enhancement effect of positive ions can increase the current density of the field emission electrons. Referring to the definition of the secondary electron emission coefficient, the emission coefficient, γ_{fe}, is obtained, such that

$$\gamma_{fe} = \frac{A_{FN} B_{FN} C_n \exp(\frac{1}{n})}{E_b^2} \exp(-\frac{D_{FN}}{E_b}) \qquad (2)$$

where D_{FN} is the threshold field strength of the field emission. The equation can be simplified to read

$$\gamma_{fe} = K \exp(-\frac{D_{FN}}{E_b}) \qquad (3)$$

where K is a function of E_b and n. Further, the parameter D_{FN} is a function of the material and surface state such that

$$D_{FN} = 6.85 \times 10^7 \frac{\varphi^{\frac{3}{2}}}{\varepsilon} \qquad (4)$$

where φ is the work function of the cathode material, and ϵ is a geometric enhancement factor for evaluating the degree on a surface.

In addition to gas ionization and secondary-electron emission, the discharge process at the microscale also includes the field emission process caused by the ion-enhanced electric field effect near the cathode surface induced by ionized

TABLE 1. Modified Paschen's law parameters.

Parameter	Physical Meaning	Value
γ_{see}	secondary electron emission coefficient	Equation(4)
K	colligation coefficient	10^7
φ	Cathode material function	5.1 （Au） 4.3 （Al） 4.6 （Ni）
$\in$	Geometric enhancement factor	50
A_{FN}	Air related constant	112.5 （kPa·cm）$^{-1}$
B_{FN}	Air related constant	2737.5V/（kPa·cm）

gas atoms. Therefore, the Thomson discharge formula needs to be modified such that

$$(\exp(\alpha g) - 1) \times (\gamma_{see} + \gamma_{fe}) \geq 1 \qquad (5)$$

where γ_{see} is the secondary electron emission coefficient. Equations (4) and (5) can be merged to produce the relation

$$\left[\gamma_{see} + K\exp\left(-\frac{gD_{FN}}{V_b}\right)\right]\left\{\exp\left[pgA_{FN}\exp\left(-\frac{pgB_{FN}}{V_b}\right)\right] - 1\right\} = 1 \qquad (6)$$

where p and V_b are defined as pressure and breakdown voltage.

Using Eq.(6), therefore, the breakdown voltage can be calculated for discharge gaps less than 10 μm, where the calculated parameter values are given in Table 1.
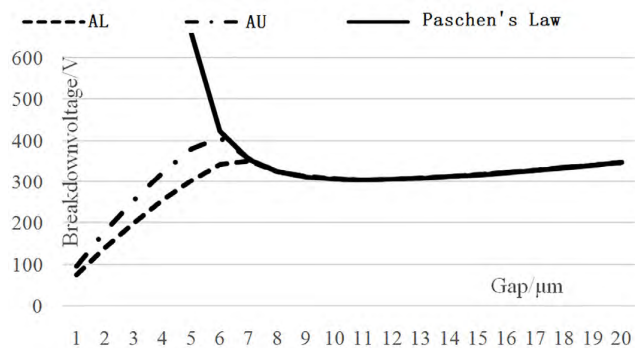

FIGURE 1. Comparison of the theoretical calculation of breakdown voltage for Al and Au electrodes and that given by Paschen's Law as a function of discharge gap distance.

The results calculated by Eq.(6) using Al and Au as electrode materials are compared in Fig. 1 with the results of the traditional Paschen's law.

As can be seen in Fig. 1, for discharge gaps larger than 5 μm the calculation results are consistent with the traditional Paschen's law. For gaps less than 5 μm, however, the calculation and the traditional Paschen's law diverge significantly.

It has been previously shown that γ_{see} has a weak correlation with external energy and ion collision angle [16]. Thus, γ_{see} is not a constant value and, at the macroscale, is affected by the gas pressure and the discharge gap distance.

The equations are considered as

$$V_B = \frac{B_{FN}pg}{\ln(pg) + k} \qquad (7)$$

$$k = \ln\left[\frac{A_{FN}}{\ln(1 + \frac{1}{\gamma_{see}})}\right] \qquad (8)$$

$$\gamma_{see} = \frac{1}{e^{\frac{A_{FN}}{e^k}} - 1} \qquad (9)$$

For air and within two set ranges of p_g, the values of k that satisfy the above relations are shown in Table 2.

TABLE 2. The value of k and pg.

pg （kPa·cm）	k
0.01~0.2	2.0583 （pg）-0.1724
0.2~100	3.5314 （pg）0.0599

For standard atmospheric pressure, the clearance value is in the range 0.01–10 μm and pg is in the range 0.01–1.0 μm. Thus, we can deduce that

$$\gamma_{see} = \frac{1}{e^{\frac{112.5}{e^{2.0583(pg)}}} - 1}. \qquad (10)$$

Comparison of the theoretical calculation and the experimental results for nickel is shown in Fig. 2 [16].
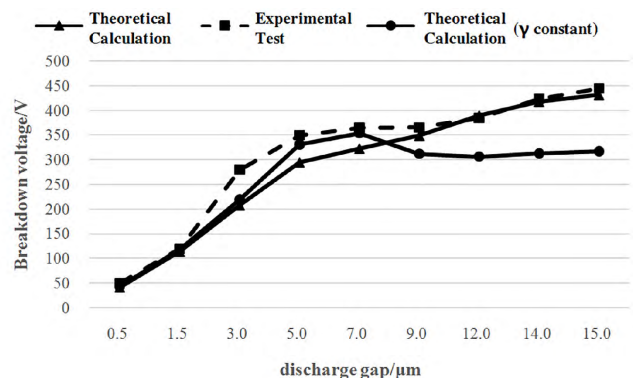

FIGURE 2. Theoretical calculation and experimental results of the breakdown voltage of a nickel electrode as a function of discharge gap distance.

According to Fig. 2, the results of the modified secondary electron emission coefficient for a gap less than 2 μm and

TABLE 3. Calculation of breakdown voltage and breakdown field strength of static conductive Al and Au structures with various discharge gap distances.

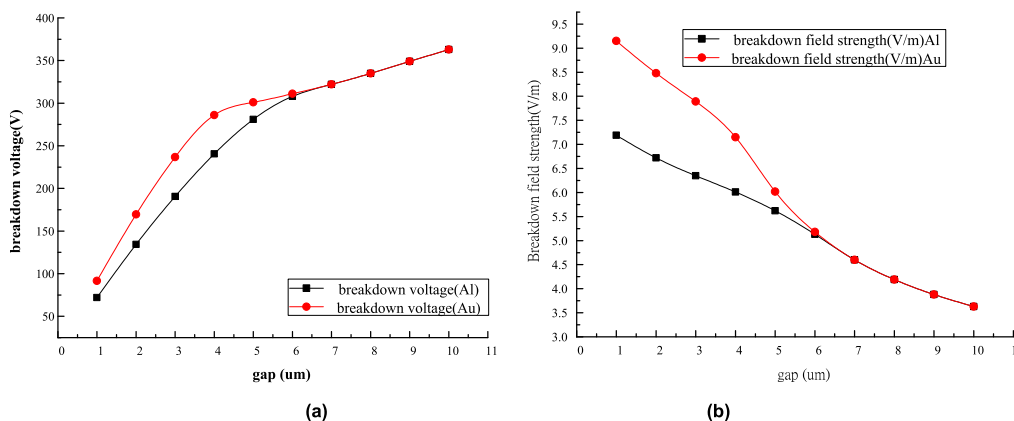| Gap/μm	breakdown voltage /V		breakdown field strength/$10^7 \cdot V \cdot m^{-1}$	
	Al	Gold	Al	Gold
1	71.9	91.5	7.19	9.15
2	134.4	169.5	6.72	8.48
3	190.6	236.8	6.35	7.89
4	240.5	286.0	6.01	7.15
5	281.0	301.0	5.62	6.02
6	308.0	311.0	5.13	5.18
7	322.0	322.0	4.60	4.60
8	335.0	335.0	4.19	4.19
9	349.0	349.0	3.88	3.88
10	363.0	363.0	3.63	3.63

FIGURE 3. Breakdown voltage (a) and breakdown field strength (b) of Al and Au electrostatic grooming structures as a function of discharge gap distance.

greater than 9 μm are in good agreement with the experimental results. Further, the deviation between the calculated and experimental results is not more than 15% between 2 and 9 μm. However, the uncorrected results show a completely different trend from the experimental results when the gap is greater than 10 μm, so the model presented in this paper is more general.

In this paper, the electrostatic grooming structure design can be dictated by Eq. (6) and (1) when γ_{see} is variable. Different electrode materials have different field-induced electron emission capabilities under the same electrostatic field environment [15], and thus herein Al and Au were used as electrode materials in the MEMS process. The gap and the predicted breakdown voltage can be calculated, as shown in Table 3.

It can be seen from Table 3 and Fig. 3 that, for Al, a small gap correlates with a lower breakdown voltage and stronger abnormal charge accumulation. However, for actual processes it is necessary to expose the electrode
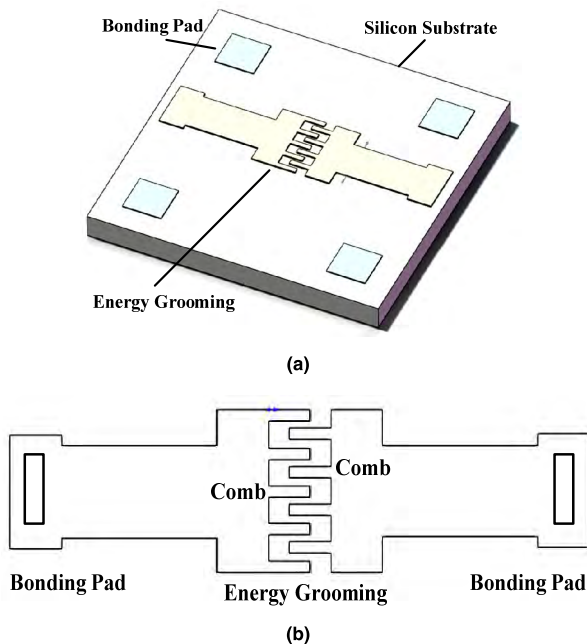
TABLE 4. Energy grooming structure dimensions.

Electrode structure feature	variable name	Value(μm)
length	l_{comb}	80
width	w_{comb}	10
Discharge gap	g_{comb}	1~10

material to air. Because Al is easily oxidized in an air environment, a significant increase in the work function will occur, which is not conducive to the grooming process. Gold, however, has high stability in an air environment and was therefore chosen herein as the electrode material. Based on the above parameters, the structure of the grooming electrode was designed to include a silicon dioxide substrate and a parallel plate electrode. The distance between the adjacent plates of the parallel electrode varied from 1 to 10 μm, where the optimum electrostatic conductivity structure was obtained by adjusting the comb gap and the

TABLE 5. Theoretical calculation and simulation results comparison of the gold electrode breakdown voltage under the same breakdown field strength.

Gap/μm	breakdown field strength /$10^7 \cdot V \cdot m^{-1}$	Theoretical calculation value /V	Simulation value /V
1	9.15	91.5	106
2	8.48	169.5	192
3	7.89	236.8	267
4	7.15	286	321
5	6.02	301	339
6	5.18	311	351
7	4.6	322	362
8	4.19	335	378
9	3.88	349	391
10	3.63	363	406

(a)

(b)

FIGURE 4. Schematics of the (a)overall structure and (b) electrostatic energy grooming based on the size effect design of Paschen's law.

electrode material. The design structure is shown in Fig. 4 and the structure dimensions of the grooming electrode are given in Table 4.

III. MULTIPHYSICS FIELD-COUPLING SIMULATIONS OF ELECTROSTATIC GROOMING SOLID-STATE PROTECTION

The multi-physics field-coupling simulations of the electrostatic grooming solid-state protection was carried out using COMSOL multiphysics field simulation software. The simulations mainly calculated the field strength of the electrostatic grooming structure for various design parameters

under various voltages and verified the theoretical calculation results. The simulations were based on the electric field intensity of varying electrode materials, electrode gaps and electrode voltages. The distribution of the electric field intensity between the comb structures for a gold electrode material, 1 μm discharge gap, and an electrode voltage ranging from 50 to 300 V is shown in Fig. 5.

As shown in Fig. 5, the tip effect causes the maximum electric field intensity to be concentrated near the tips of the electrostatic grooming solid-state protection comb, which is also the location of the initial electrostatic breakdown. The simulation results under different conditions are given in Table 5.

It can be seen from Fig. 6 that the edge effect of the electrode and the effect of the electric field concentration at the structure tip are considered in the simulation process. The electric field intensity between the comb and the applied electrode voltage does not follow a strictly linear relationship, but the overall trend still satisfies a linear variation. A comparison of the results of simulations and calculations under the same breakdown electric field are gathered in Table 5. Through data fitting, a comparison between the theoretical calculation and the simulation results of the breakdown voltage can be found, which is shown in Fig. 7.

According to Fig. 7, the breakdown trend is more obvious for discharge gap distances of 1–4 μm than for gap distances of 4–10 μm gap. Further, the breakdown voltage obtained via simulation was greater than that obtained via theoretical calculation, where the average deviation between the theoretical calculation and simulation is 12.87%, which satisfies the allowable range. According to the theoretical calculation and the simulation, the structure can be determined and the process mechanism can be understood.
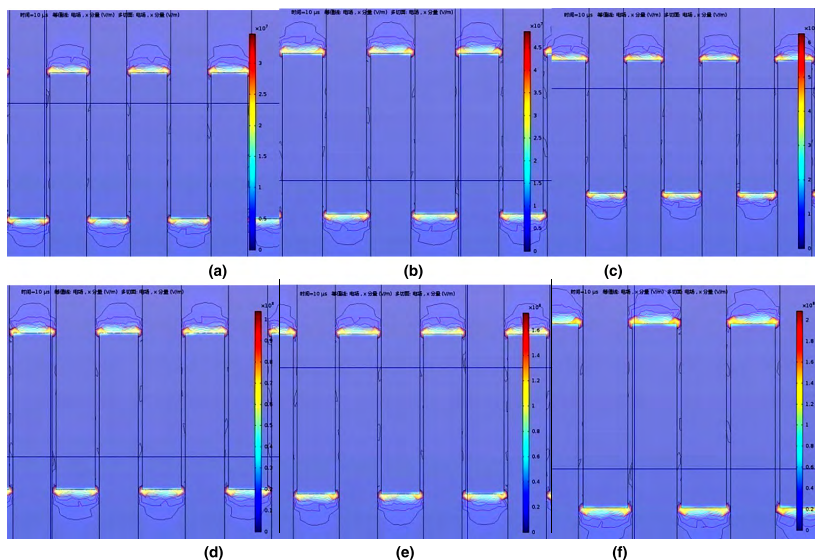
FIGURE 5. Distribution of the electric field intensity for an electrode voltage of (a) 50, (b) 70, (c) 90, (d) 150, (e) 250 and (f) 300 V with Au as the electrode material and a discharge gap of 1 μm.
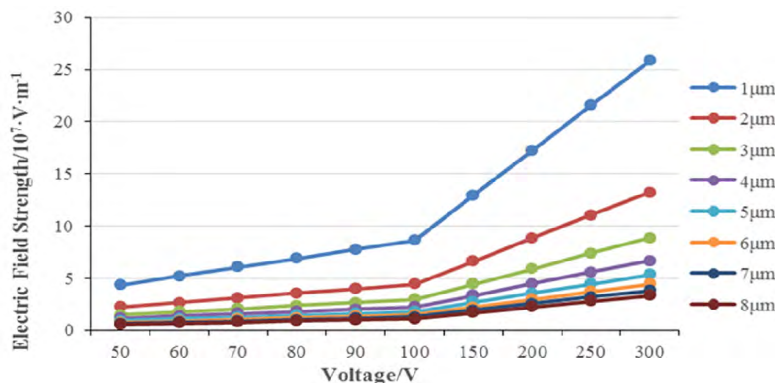

FIGURE 6. Electric field strength of the Au electrode as a function of electrode voltage for various discharge gap values.
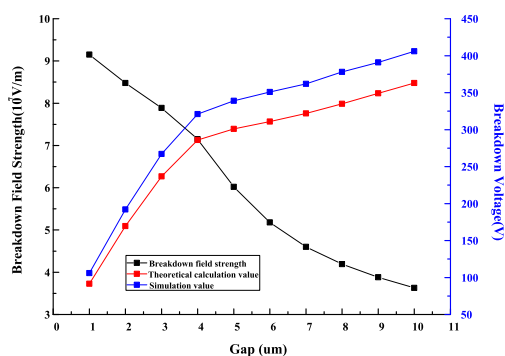

FIGURE 7. Comparison the Au electrode breakdown voltage as a function of discharge gap obtained via theoretical calculation (red squares, right axis) and by simulation (blue squares, right axis) under the same breakdown field strength (black squares, left axis).

It can be seen from Table 5 that the deviation between the theoretical calculation results and the simulation results is less than 20%, which verifies the correctness of the theoretical calculation and simulation.

IV. FABRICATION PROCESS FOR THE ENERGY GROOMING STRUCTURE

Deep reactive ion etching (inductively coupled plasma (ICP) etching) of bulk silicon will inevitably reduce the surface smoothness of the device, thus creating structural inflection points in the etching region that will induce static electricity accumulation. A stable energy grooming function cannot be realized at the structure discharge tip, and therefore the electrostatic energy grooming design herein adopted a silicon-based surface technology. Because different electrode materials have different energy grooming capabilities under the same electrostatic environment, simulations of multiple physical fields were also carried out. The twelve steps of the process flow for the fabrication of the energy grooming structure used herein are as follows (Fig. 8):

A. The Si(100) substrate was prepared;

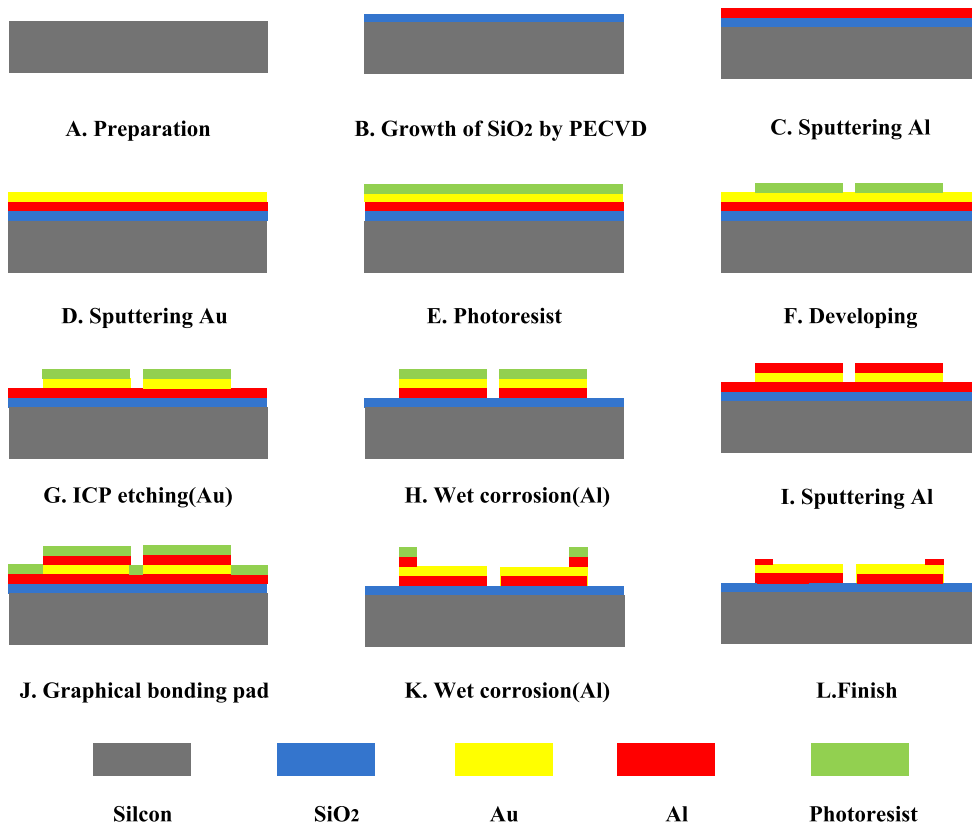B. Silicon oxide 500 nm-thick was grown on the Si(100) substrate using thermal oxygen;

A. Preparation | B. Growth of SiO2 by PECVD | C. Sputtering Al

D. Sputtering Au | E. Photoresist | F. Developing

G. ICP etching(Au) | H. Wet corrosion(Al) | I. Sputtering Al

J. Graphical bonding pad | K. Wet corrosion(Al) | L.Finish

Silcon | SiO2 | Au | Al | Photoresist

FIGURE 8. Process flow for the fabrication of the energy grooming structure.

C. Al (1 μm thick) was sputtered on the metal substrates to graphically form discharge electrodes;

D. Au (50 nm thick) was sputtered on the Al-coated substrates;

E–F. Photoresist (AZ6130) was deposited and developed, where the graphic photoresist had a development time of 45 s;

G. ICP etching of Au.

H. Wet etching of Al, where the etching solution formula was as follows:

$V_{CH_3COOH} : V_{HNO_3} : V_{H_2O} : V_{H_3PO_4} = 1 : 1 : 2 : 16$, with a corrosion rate of 135 nm/min, temperature of 70°, and duration of 3 min and 10 s

I–K. Sputter-deposition of Al (300 nm thick) on the metal substrates, graphically forming the discharge electrode pad;

L. Photoresist removal, cleaning, and energy grooming structure processing.

Fig. 9 shows a field emission scanning electron microscope image of the energy grooming structure where it can be seen that the electrode material stripped by wet etching process roughens the edge of the electrode, creating small protrusions. These protrusions may lead to a local inhomogeneity of the electric field, which may result in an inconsistency between the breakdown voltages obtained experimentally and those calculated theoretically.

For ease of testing, the processed wafer was diced and a chip-on-board (COB) package was assembled on a single chip, as shown in Fig. 10.

V. TESTING

The optical microscope image of the chip after COB assembly (Fig. 11) shows that the bonding line is a 50 μm high-power gold wire with a 10 mm-long fuse current over 1 A, which prevents a failure of the bonding line from impacting the grooming effect.

Each chip possessed two independent electrostatic hydrophobic structures, and the two grooming structures in the same chip had the same structure and size. It can be seen in Fig. 11 that the chip edge exhibits a certain degree of deformation and surface material shedding owing to dicing, but the functional area of the chip is complete and can adequately meet the needs of the test.

Herein, the fuse micro-electrostatic grooming solid-state protection test was based on a self-developed DC high-voltage generator, where the test system is schematically shown in Fig. 12.

As shown in Fig. 12, the testing was divided into the two components of charging and discharging. The charging circuit included a DC high-voltage generator, a 2200 μF
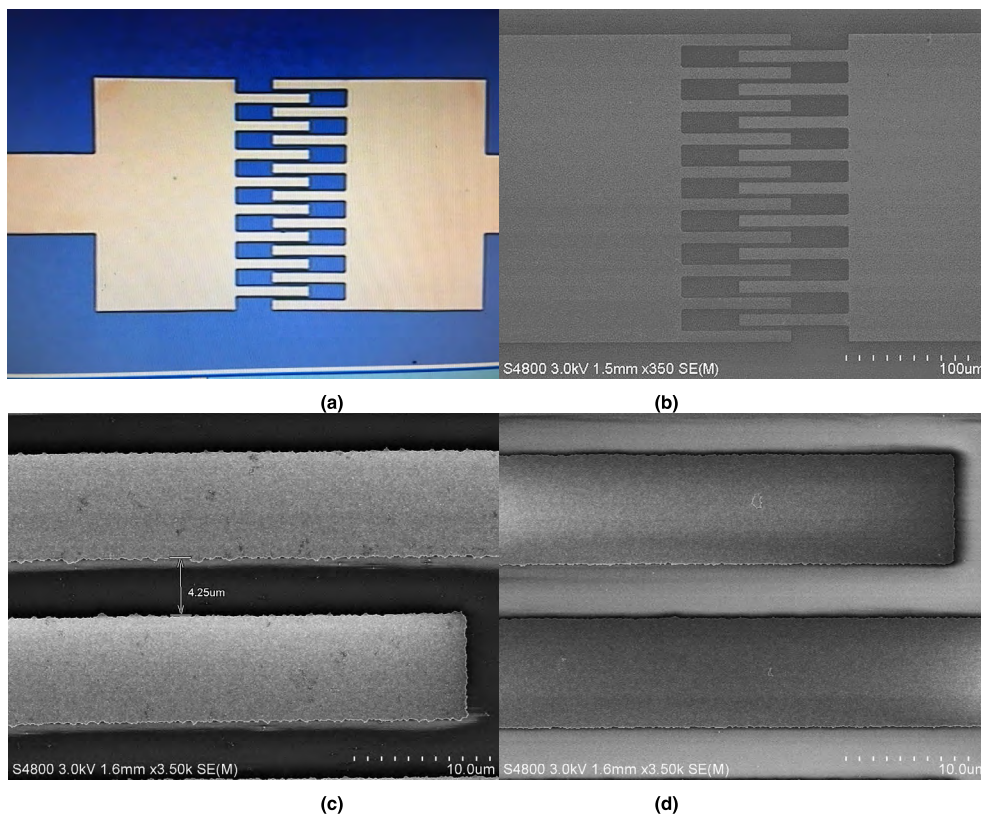
FIGURE 9. Energy grooming structure morphology using (a) optical microscopy and (b, c, d) field-emission scanning electron microscopy.
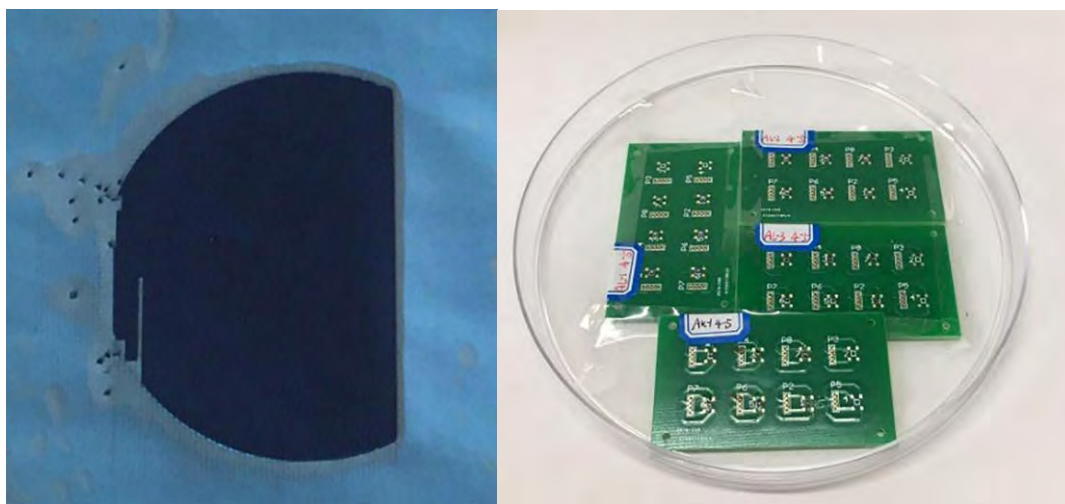

FIGURE 10. Optical images of the electrostatic grooming structure after dicing (left image) and chip-on-board assembly (right image).

charge resistor, an energy storage capacitor and a charging switch. The DC high-voltage generating device could generate a 310 V DC pulsed high voltage, while the charging resistor was used for current limiting so that the DC high-voltage generating device and the energy storage capacitor were prevented from being excessively burnt by the charging current. The discharging circuit included a 500 Ω capacitor, a current-limiting resistor, a discharging switch and the electrostatic grooming solid state protection structure.
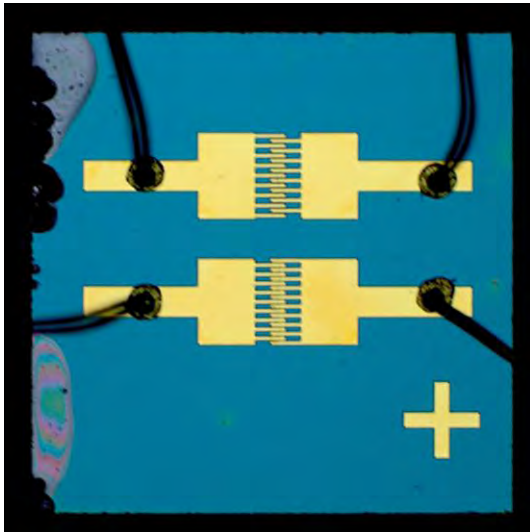
FIGURE 11. Optical microscope image of electrostatic grooming structure, where the bonding lines are at both ends of the electrode.

FIGURE 12. Schematic diagram of the electrostatic grooming structure testing system.

A complete test consisted of two processes: charging and discharging. When charging, the discharging switch was opened and the charging switch was closed. The DC high-voltage generator charged the energy storage capacitor via the charging resistance, and the voltage at both ends of the energy storage capacitor could be measured by the voltmeter. During discharge, the charging switch was opened and the discharging switch was closed, whereupon the voltage at the two ends of the energy storage capacitor were connected to the two ends of the electrostatic grooming solid state insurance. In this configuration, the current limiting resistance prevented circuit burnout owing to excessive current at the moment of breakdown.

The breakdown process is greatly affected by the atmospheric pressure and temperature, and all experiments herein were carried out at room temperature (20°C) and at atmospheric pressure (101.325 kPa). The breakdown voltages of

gaps varying from 1 to 6 μm were measured by means of the lifting method. The experimental results show that the electrostatic grooming with certain gap distances will cause a breakdown of the air between the electrodes at a certain voltage, accompanied by obvious luminescence and sound. The experimental results are shown in Fig. 13.

From Fig. 13, it can be seen that, even with the presence of current limiting in the discharge circuit, the breakdown process still induces a violent phase transition reaction in the electrode material, resulting in melting of the electrode. The electrodes exhibited both partial and complete melting, which is mainly owing to the fact that the comb gap in the same grooming structure is not completely consistent because of the device process. When the device process difference is large, the deviation between the gaps can reach 30%, which results in the uneven field strength among the comb structures. Using calculations, the reliable breakdown voltage for each discharge gap distance value is given in Table 6.
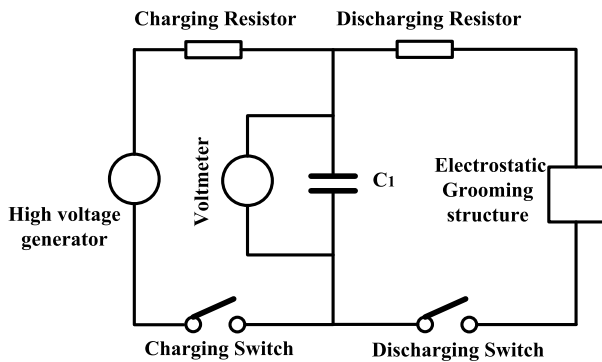
TABLE 6. Test breakdown voltage and calculated breakdown values for electrostatic structure tests for various discharge gap distances.

Gap/μm	Calculated Values/V	Test breakdown voltage/V
1	91.5	128.3
2	169.5	181.4
3	236.8	229.2
4	286.0	245.3
5	301.0	269.4
6	311.0	277.2

It can be seen from Table 6 that the theoretical calculations of the breakdown voltage for the various discharge gap distances are relatively close to those of the test results, where the deviation is larger for larger gaps and is smaller for smaller gaps. The main reason for the discrepancy is the poor clearance accuracy control in the process. The relative gap deviation is large for small gaps, so the actual gap used to measure the breakdown is not strictly 1 μm, but has a relative deviation of about 25%. As the gap distance increases, the absolute deviation of the gap process does not change and thus the relative deviation is reduced, so that the measured value is closer to the theoretical calculation value.

The above experiments verify the validity and accuracy of the theoretical calculation, and that the electrostatic conductivity solid-state protection has the ability of reliable electrostatic charge conduction.

The static voltage guidance of different threshold voltages can be realized by controlling the comb clearance (i.e., discharge gap). In this way the minimum effective guide voltage
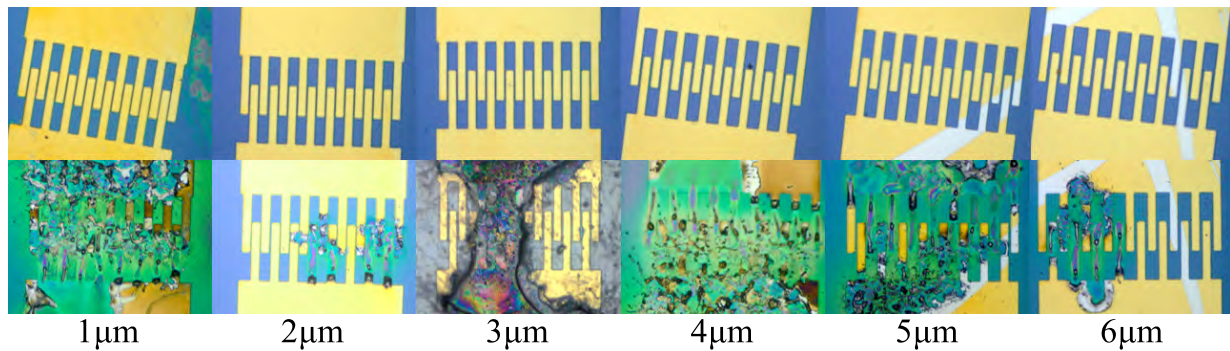
FIGURE 13. Comparison of device morphology before (upper row) and after (lower row) breakdown testing for an electrode gap of (a) 1μm, (b) 2μm, (c) 3μm, (d) 4μm, (e) 5μm and (f) 6μ.

can be reduced to 130 V, which can significantly improve the safety of the electrostatics.

VI. CONCLUSION

Herein, a microscale breakdown model based on field emission and secondary electron emission coefficients is proposed. The model is in good agreement with the experimental results in the discharge gap distance range of less than 2 μm and more than 9 μm. In the discharge gap range of 2–9 μm, the deviation of the test results is less than 15%. The model has excellent adaptability in the global range. Based on the above model, the influence of various materials and the discharge gap on the hydrophobic effect is analyzed. Finally, gold is selected as the electrode material.

Subsequently, this paper carried out multiphysics field simulation analysis based on COMSOL. Under the same breakdown field strength, the deviation between the theoretical calculation and the simulation is not more than 20%, which verifies the accuracy of the simulation results.

Using these results, a 4-inch silicon wafer is used to process electrostatic conductive solid-state protection, and the chip is encapsulated and tested via COB. The breakdown voltage of a gold comb electrode with a gap varying from 1 to 6 μm is obtained using the lifting method. The deviation between the calculated results and the theoretical results is less than 25%, which verifies the correctness of the theory.

The experimental results show that the electrostatic hydrophobic solid-state protection based on the size effect of Paschen's law can effectively groom an electrostatic charge above 130 V. In other words, the static charge can be effectively released prior to an electrostatic excitation of the initiator, and the electrostatic resistance of the initiator can thus be improved.

REFERENCES

[1] T. L. King, "Pin-to-pin electrostatic discharge protection for semiconductor bridges," Sandia Nat. Lab., Albuquerque, NM, USA, Tech. Rep. SAND2002-2213, Jul. 2002.

[2] J. Weinlein, D. Sanchez, and J. Salas, "Electrostatic discharge (ESD) protection for a laser diode ignited actuator," Sandia Nat. Lab., Albuquerque, NM, USA, Sandia Rep. SAND2003-2100, Jun. 2003.

[3] C.-H. Chen, J. A. Yeh, and P.-J. Wang, "Electrical breakdown phenomena for devices with micron separations," *J. Micromech. Microeng.*, vol. 16, no. 7, pp. 1366–1373, Jul. 2006.

[4] M. D. Hogue, R. E. Cox, J. Mulligan, K. Ahmed, J. G. Wilson, and L. M. Calle, "Dynamic gas flow effects on the ESD of aerospace vehicle surfaces," *J. Electrostatics*, vol. 91, pp. 21–27, Feb. 2018.

[5] D. Bouangeune, S. Vilathong, D.-H. Cho, K.-H. Shim, S.-J. Leem, and C.-J. Choi, "Novel punch-through diode triggered SCR for low voltage ESD protection applications," *J. Semicond. Technol. Sci.*, vol. 14, no. 6, pp. 797–801, Dec. 2014.

[6] D. Bouangeune, S.-S. Choi, C.-J. Choi, D.-H. Cho, and K.-H. Shim, "Bidirectional transient voltage suppression diodes for the protection of high speed data line from electrostatic discharge shocks," *J. Semicond. Technol. Sci.*, vol. 14, pp. 1–7, Feb. 2014.

[7] J. A. Salcedo, J.-J. Hajjar, S. Malobabic, and J. J. Liou, "Bidirectional devices for automotive-grade electrostatic discharge applications," *IEEE Electron Device Lett.*, vol. 33, no. 6, pp. 860–862, Jun. 2012. doi: 10.1109/LED.2012.2190261.

[8] Z. Liu, J. Vinson, L. Lou, and J. J. Liou, "An improved bidirectional SCR structure for low-triggering ESD protection applications," *IEEE Electron Device Lett.*, vol. 29, no. 4, pp. 360–362, Mar. 2008.

[9] D. Bouangeune, D.-H. Cho, H.-J. Yun, K.-H. Shim, and C.-J. Choi, "Transmission line pulse properties for a bidirectional transient voltage suppression diode fabricated using low-temperature epitaxy," *Electron. Mater. Lett.*, vol. 11, pp. 88–92, Jan. 2015.

[10] D. Bouangeune, W.-K. Hong, S.-S. Choi, C.-J. Choi, D.-H. Cho, J. M. Park, J. H. Lee, H.-D. Yang, and K.-H. Shim, "ESD robustness of low-voltage/high-speed TVS devices with epitaxial grown films," in *Proc. IEEE 1st Global Conf. Consum. Electron.*, Oct. 2012, pp. 189–192.

[11] M. Mardiguian, *Electrostatic Discharge: Understand, Simulate and Fix ESD Problems*, 3rd ed. Hoboken, NJ, USA: Wiley, 2009, ch. 1, p. 30.

[12] F. Liu, S. Gao, H. Han, Z. Tian, and P. Liu, "Interference reduction of high-energy noise for modal parameter identification of offshore wind turbines based on iterative signal extraction," *Ocean Eng.*, vol. 183C, pp. 372–383, 2019.

[13] Z. Li, K. Goebel, and D. Wu, "Degradation modeling and remaining useful life prediction of aircraft engines using ensemble learning," *ASME Trans. J. Eng. Gas Turbines Power*, vol. 141, Nov. 2018, Art. no. 041008.

[14] R. Chundru, Z. Li, D. Pommerenke, K. Kam, C.-W. Lam, F. Centola, and R. Steinfeld, "An evaluation of TVS devices for ESD protection," in *Proc. IEEE Int. Symp. Electromagn. Compat.*, Long Beach, CA, USA, 2011, p. 62.

[15] D. B. Go and A. Venkattraman, "Microscale gas breakdown: Ion-enhanced field emission and the modified Paschen's curve," *J. Phys. D, Appl. Phys.*, vol. 47, no. 50, Nov. 2014, Art. no. 503001.

[16] R. H. Fowler and L. Nordheim, "Electron emission in intense electric fields," *Proc. R. Soc. Lond. A, Math. Phys. Sci.*, vol. 119, no. 781, pp. 173–181, May 1928.

[17] M. A. Beamesderfer, S. Chen, D. L. DeVoe, E. Litcher, and K. Johnson, "Analysis of an optical energy interrupter for MEMS-based safety and arming systems," *Proc. SPIE*, vol. 3880, pp. 11–101, Aug. 1999.

[18] E. Husain and R. S. Nema, "Analysis of paschen curves for air, N2 and SF6 using the townsend breakdown equation," *IEEE Trans. Electr. Insul.*, vol. EI-17, no. 4, pp. 350–353, Aug. 1982.

HENGZHEN FENG (M'17) was born in Inner Mongolia, China, in 1991. He received the B.S. and M.S. degrees in instrument science and technology from the North University of China. He is currently pursuing the Ph.D. degree with the Beijing Institute of Technology, China.

From 2013 to 2017, he was the author of seven articles and three inventions. His research interests include high-pressure, and high-overload accelerometer designs, processes and applications. He is involved in the design and application of micro actuators in high dynamic environments.

WENZHONG LOU was born in Shanxi, China, in 1969. He received the B.S., M.S., and Ph.D. degrees in mechanical engineering from the Beijing Institute of Technology, in 1996 and 2001.

He served as the Director of the Chinese Society of Micro-Nano Technology. Since 2009, he has been involved in the research of mechatronical engineering and micro-electromechanical system (MEMS). In the past five years, he has completed five monographs, and he finished four textbooks and two translations. He is currently with the National Key Laboratory of Electro-Mechanics Engineering and Control, School of Mechatronical Engineering, Beijing Institute of Technology. He had published more than 110 academic papers in related fields, of which more than 80 are included in SCI and EI. He holds over 40 authorized invention patents.

He is a member of the International IEC Standard TC47 and the Editorial Board Member of the *Journal of Detection and Control*. He served as an Executive Editor for series books of modern mechatronical engineering technology, which received funding from the China National Publishing Fund.

FUQUAN ZHENG was born in Shandong, China, in 1994. He received the B.S. degree in mechanical engineering from the North University of China, in 2017. He is currently pursuing the M.S. degree in mechanical engineering with the Beijing Institute of Technology.

Since 2017, he has been involved in the research of mechatronical engineering and micro-electromechanical system (MEMS). He had published five academic papers in related fields. His research interest includes the development of surface processing techniques.

XURAN DING (M'17) was born in Inner Mongolia, China, in 1989. He received the B.S. and M.S. degrees from the School of Mechatronical Engineering, Beijing Institute of Technology, China, in 2018, where he is currently pursuing the Ph.D. degree.

He is currently with China North Industries Corporation. From 2012 to 2018, he was the author of eight articles and 16 inventions. His research interests include micro actuators and micro switches in high-pressure and high-overload environments.

● ● ●